Supplemental data

Figure S1

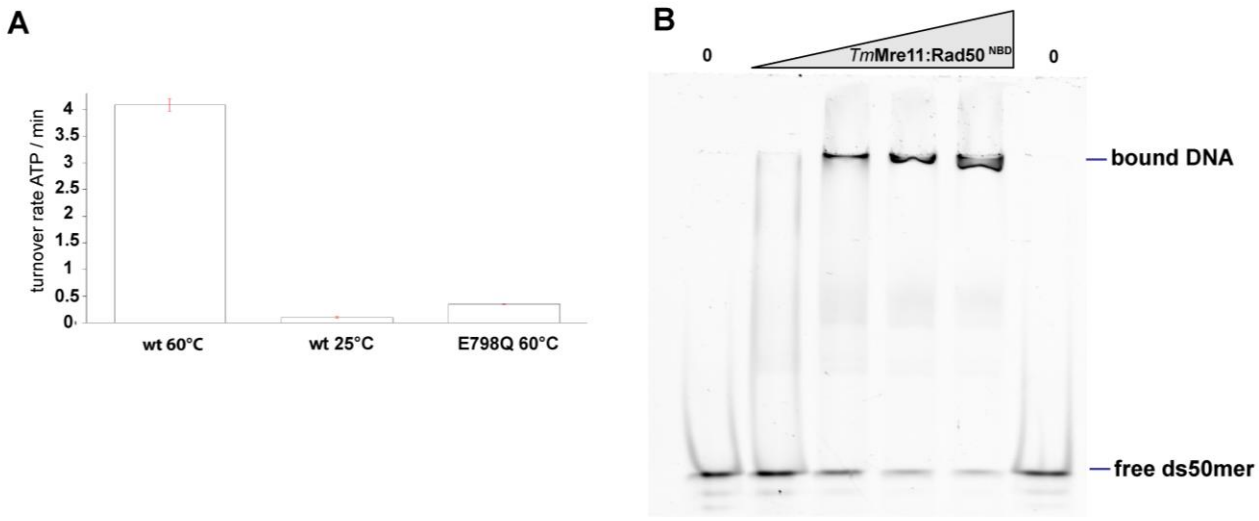

Figure S1: ATPase and DNA binding activity of *Tm*MR^{NBD}, related to Figure 1.

A) ATP hydrolysis activity of thermophilic *Tm*MR^{NBD} (wt) at 60°C or 25°C. A Walker B motif mutant (E798Q) in *Tm*Rad50 rules out contaminating activities. Error bars depict +/- standard deviation of three independent experiments.

B) DNA binding activity of *Tm*MR^{NBD} using electrophoretic mobility shift assay. Following protein concentrations (0, 0.5, 2.0, 4.0 and 6.0 µM respectively) were analyzed.

Figure S2

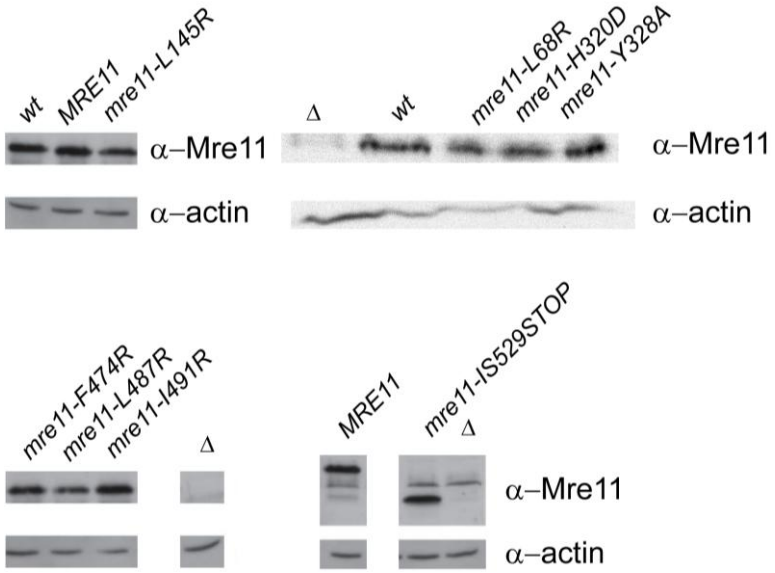

Figure S2: Western blot analysis of protein levels for different Mre11 mutants show that all mutant proteins are produced at normal endogenous levels. Endogenous actin is used as loading control. Related to Figure 2.

Figure S3

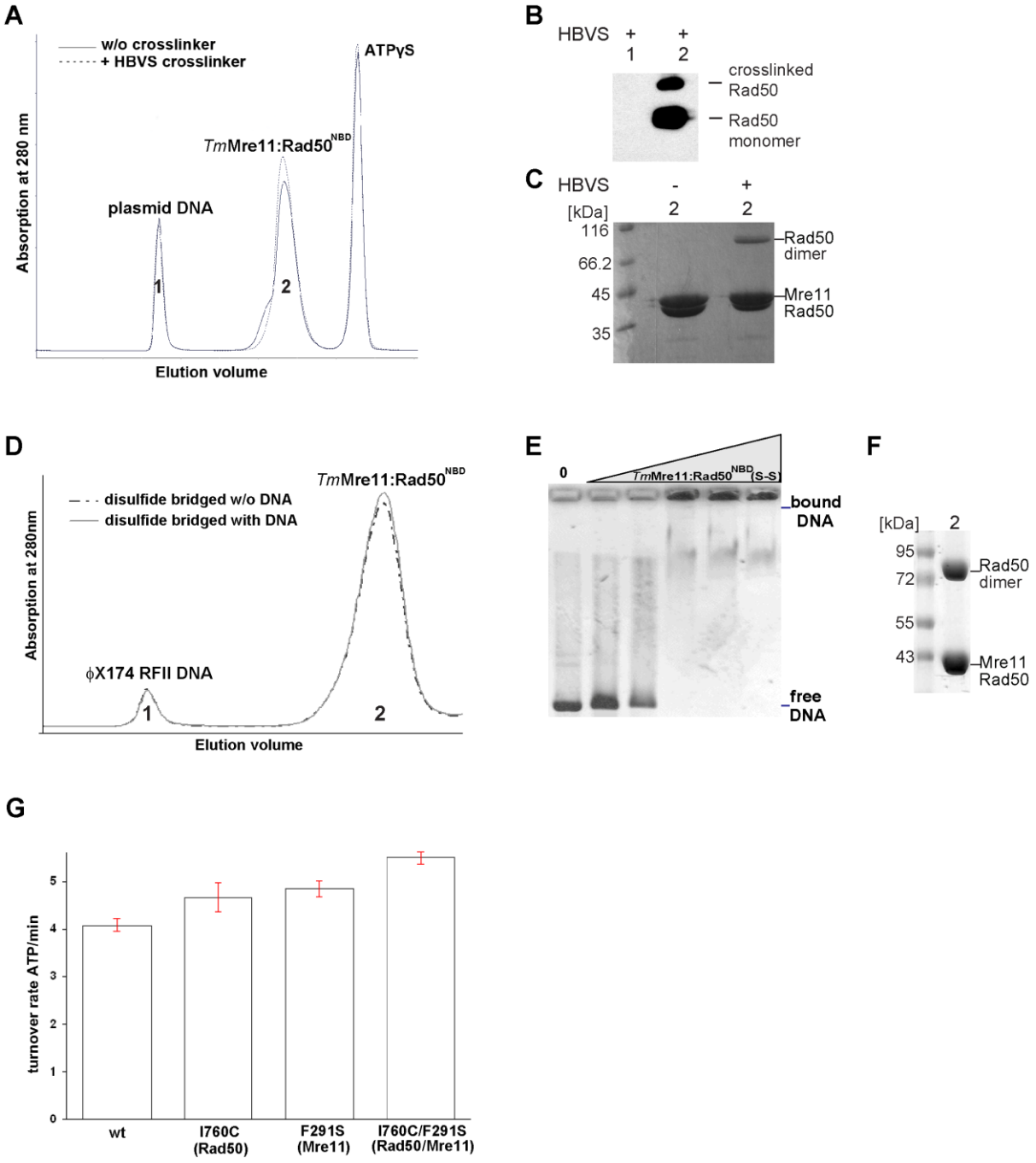

Figure S3: Biochemical analysis of *Tm*MR^{NBD} complexes, related to Figure 3.

A) Gel filtration chromatogram of the Mre11:Rad50^{NBD} complex in presence of ATPγS and pBS II KS+ plasmid DNA (solid line). The dashed line shows the chromatogram for the complex treated with HBSV crosslinker in the presence of DNA and ATPγS prior to gel filtration. The UV absorption peaks corresponding to the $Mre11_2$:$Rad50^{NBD}{}_2$ complex shows no change in elution volume, indicating that NBDs from the same complex are crosslinked

but not NBDs from different complexes. Latter should result in heterooctamers with increased hydrodynamic radii.

B) Western blot analysis of the fractions 1 and 2 of A) with an α-His antibody against His-tagged Rad50^{NBD}. Fraction 2 contains both the uncrosslinked and crosslinked Mre11:Rad50^{NBD} complex. We do not see crosslinked Mre11:Rad50^{NBD} co-eluting with the plasmid DNA fraction, indicating that *Tm*Mre11:Rad50^{NBD} cannot be crosslinked as a stable "ring" around internal DNA.

C) SDS polyacrylamide gel showing the amount of crosslinked *Tm*Rad50^{NBD}.

D) Gel filtration chromatogram of the disulfide bridged Mre11:Rad50^{NBD} complex in the presence of ATP and ΦX174 RF II plasmid DNA. Disulfide bridging of the complex was carried out either in the presence (solid line) or absence (dashed line) of DNA, prior to gel filtration. We do not see disulfide bridged Mre11:Rad50^{NBD} co-eluting with the plasmid DNA fraction (peak 1), indicating that *Tm*Mre11:Rad50^{NBD} cannot form a stable "ring" around internal DNA.

E) DNA binding activity of the disulfide bridged *Tm*Mre11:Rad50^{NBD} tested by electrophoretic mobility shift assay shows, that the ΦX174 RFII plasmid DNA was completely bound by the complex at concentrations used in the above described gel filtration chromatography experiment (Fig. S3).

F) SDS polyacrylamide gel showing the disulfide bridged *Tm*Rad50^{NBD} complex from peak 2 of the gel filtration chromatogram.

G) ATP hydrolysis activity of three interface 2 mutant *Tm*Mre11:Rad50^{NBD} protein complexes compared to wildtype (wt) activity at 60°C. The I760C^{Rad50} mutant as well as the F291S^{Mre11} mutant possess a slightly increased ATPase activity (116% and 121% compared to wt respectively), whereas the I760C ^{Rad50} F291C ^{Mre11} shows 130% of the wt activity. Error bars depict +/- standard deviation of three independent experiments.

Figure S4

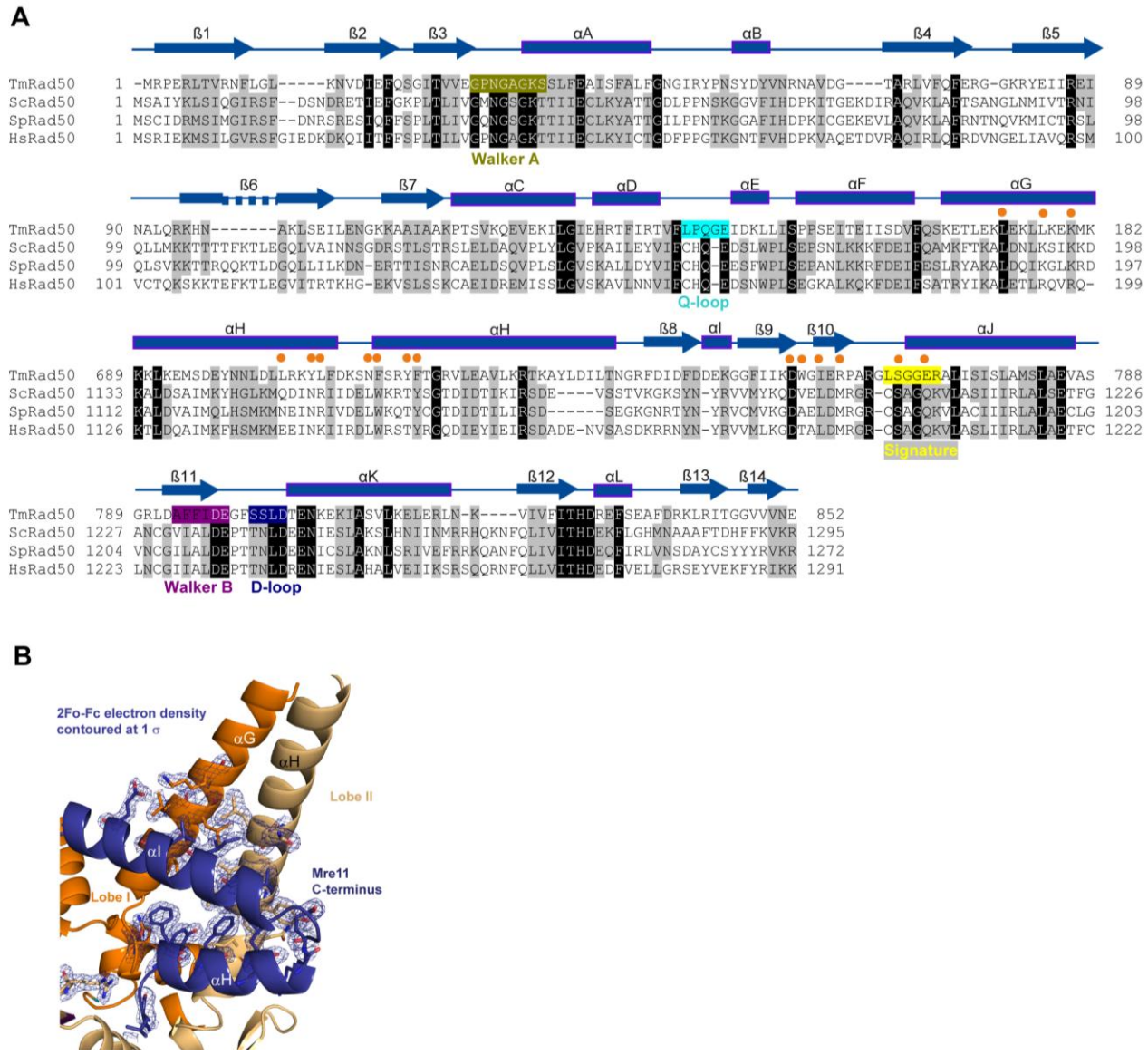

Figure S4: Sequence alignment of the Rad50^{NBD} domain and detailed view of the Mre11^{HLH} and Rad50^{NBD} interaction, related to Figure 4.

A) Sequence alignment of the Rad50 NBD domain (M1-K182 and K689-E852). Conserved residues are shown in black and grey, corresponding to their level of conservation. Rad50^{NBD} residues involved in the Mre11:Rad50^{NBD} Interface 1 and 2 (Fig. 2B1, 2B2) are marked via orange dots.

B) Detailed view of the Mre11 helix-loop-helix (HLH) motif (blue) and its interaction with the base of the Rad50 coiled-coil (orange and yellow) (taken from the higher resolved AMPPNP complex structure). Selected side chains are shown as color-coded sticks and the 2Fo-Fc electron density map contoured at 1.0 σ, is shown around the interacting residues.

Figure S5

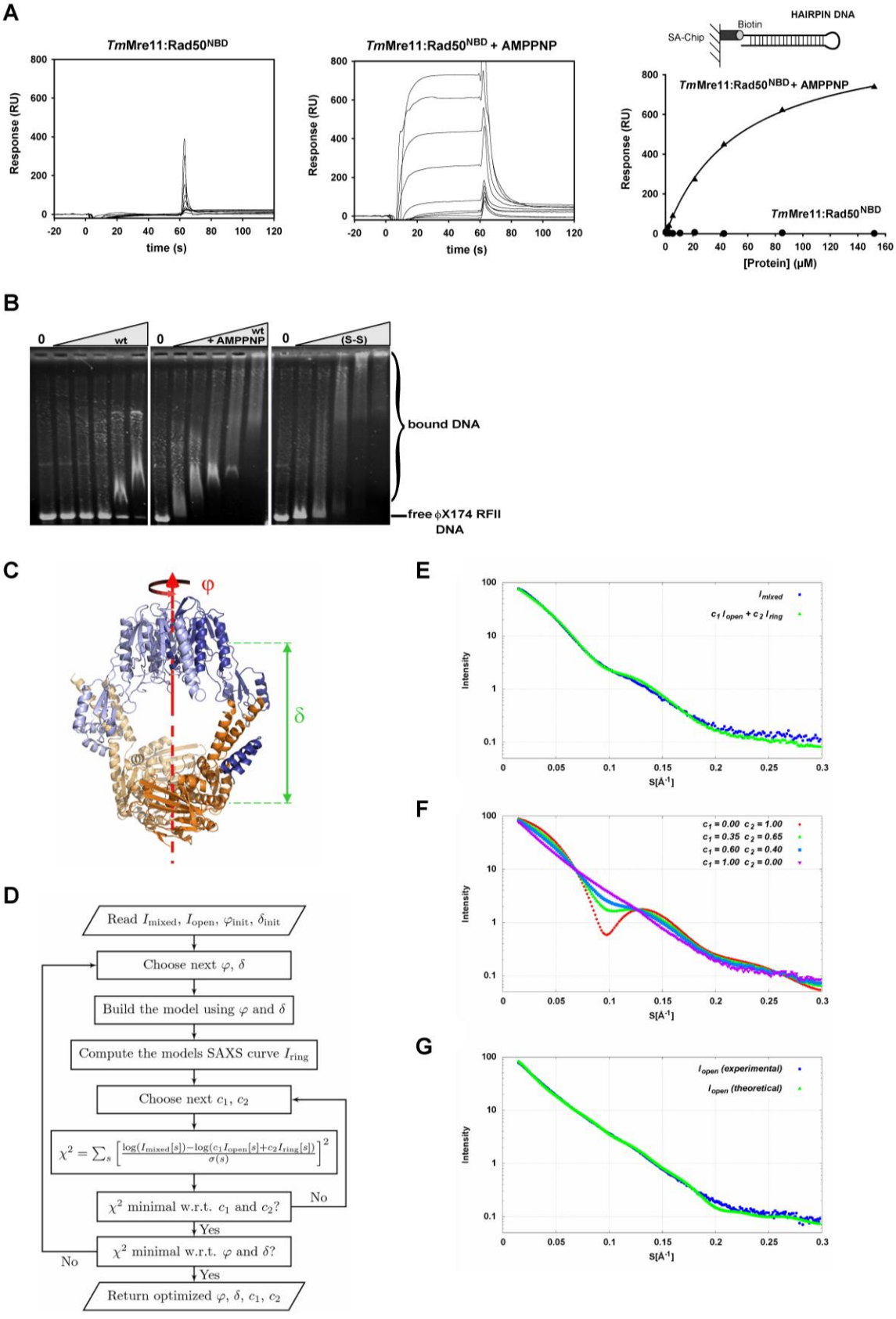
A
TmMre11:Rad50NBD
TmMre11:Rad50NBD + AMPPNP
HAIRPIN DNA
Biotin
SA-Chip
TmMre11:Rad50NBD+ AMPPNP
TmMre11:Rad50NBD
Response (RU)
time (s)
[Protein] (μM)
B
wt
+ AMPPNP
(S-S)
bound DNA
free ϕX174 RFII DNA
C
φ
δ
D
Read I_{mixed}, I_{open}, φ_{init}, δ_{init}
Choose next φ, δ
Build the model using φ and δ
Compute the models SAXS curve I_{ring}
Choose next c_1, c_2
$\chi^2 = \sum_s \left[\frac{\log(I_{mixed}[s]) - \log(c_1 I_{open}[s] + c_2 I_{ring}[s])}{\sigma(s)}\right]^2$
χ^2 minimal w.r.t. c_1 and c_2?
No
Yes
χ^2 minimal w.r.t. φ and δ?
No
Yes
Return optimized φ, δ, c_1, c_2
E
I_{mixed}
$c_1 I_{open} + c_2 I_{ring}$
Intensity
S[Å^{-1}]
F
$c_1 = 0.00$ $c_2 = 1.00$
$c_1 = 0.35$ $c_2 = 0.65$
$c_1 = 0.60$ $c_2 = 0.40$
$c_1 = 1.00$ $c_2 = 0.00$
G
I_{open} (experimental)
I_{open} (theoretical)

Figure S5: DNA binding activity and model of the "closed" *Tm*MR^{NBD} complex, related to Figure 6.

A) SPR sensograms showing the binding of *Tm*MR^{NBD} to a hairpin DNA immobilized on a SA-sensor chip w/wo 5 mM AMPPNP. The protein was injected at concentrations of 0, 0.66, 1.3, 2.7, 5.3, 10.6, 21.2, 42.5, 85 and 154 µM. SPR measurements were performed as described in Supplemental Data. The third diagram shows the comparison of the hairpin DNA binding of the *Tm*MR^{NBD} in absence (●) and presence (▲) of AMPPNP.

B) DNA binding affinity to ds ΦX174 RF II plasmid DNA of the wildtype *Tm*MR^{NBD} complex w/o AMPPNP compared to the disulfide bridged *Tm*MR^{NBD} (S-S) complex without ATP analog tested by electrophoretic mobility shift assay. The EMSA indicates that the closed, ATP bound complex resembles the DNA binding conformation.

C) The closed state model is built from the structures of the Rad50 dimer and the Mre11 dimer. Their C2 symmetry axes are assumed to coincide, which reduces the free parameters to just two: the distance δ between their centers of mass and the rotation angle of the Rad50 dimer with respect to the Mre11 dimer.

D) Flow chart describing the procedure to fit the model parameters δ and φ as well as the mixture coefficients c_1 and c_2 to the experimental SAXS curve for the "open" complex and the curve for the mixture of "open" and "closed" state complexes.

E) The fit procedure minimizes χ^2, the sum of squared deviations of the experimental curve for the mixed conformation (blue trace) from the curve of the mixed configuration calculated using the closed state model (green trace). The agreement of experimental and theoretical curves is fairly close, except at small scattering angles ($s > 0.2$ Å^{-1}).

F) SAXS curves calculated with CRYSOL for mixtures of open and closed state complexes with different fractions of "open" and "closed" states (c_1 and c_2, respectively). A comparison with the blue trace in E shows that the fraction of closed state complex is approximately 40% for the blue trace.

G) The error model $\sigma(s)$ is derived from the log deviation of the experimental SAXS curve (blue trace) and the theoretical SAXS curve (green trace) of the crystallized open state complex.